Volume 54 | Number 37 | 7 May 2018 | Pages 4635–4730

ChemComm

Chemical Communications

rsc.li/chemcomm

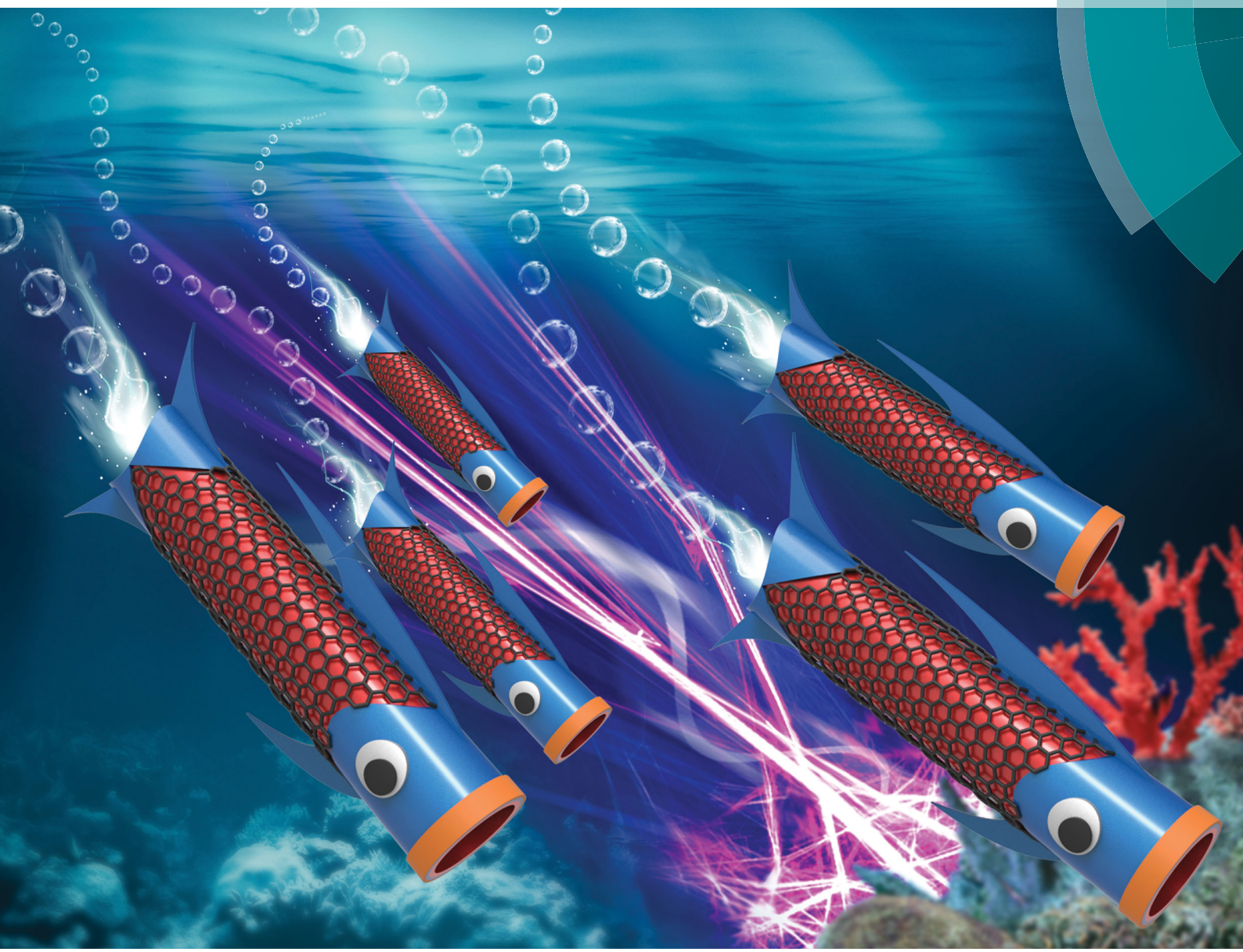

ISSN 1359-7345

ROYAL SOCIETY OF CHEMISTRY

COMMUNICATION

Hongqi Sun, Shaobin Wang *et al.*

Pt-Free microengines at extremely low peroxide levels

ChemComm

COMMUNICATION

View Article Online
View Journal | View Issue

Cite this: *Chem. Commun.*, 2018, 54, 4653

Received 24th February 2018,
Accepted 29th March 2018

DOI: 10.1039/c8cc01548a

rsc.li/chemcomm

Pt-Free microengines at extremely low peroxide levels†

Heng Ye,[a] Guofeng Ma,[b] Jian Kang,[a] Hongqi Sun *[c] and Shaobin Wang *[a]

Herein, we demonstrate that iron oxide modified MnO_2 (FeO_x–MnO_2) catalyzed micromotors can be fabricated *via* electrochemical co-reduction and exhibit exceptional high performance at an extremely low hydrogen peroxide (H_2O_2) fuel concentration. We observed that graphene/FeO_x–MnO_2 microtubes could show motion behaviors at fuel concentration as low as 0.03% H_2O_2, which is nearly one order of magnitude lower than Pt-based micromotors (normally at above 0.2% H_2O_2). Moreover, the micromotors exhibit higher speeds than any other reported catalytic micro/nanomotors (MNMs) at low peroxide levels. The FeO_x–MnO_2 systems are better catalytic MNMs, due to their excellent catalytic activity, easy fabrication, robust structure and movement, as well as low-cost, biocompatible and abundance nature, showing great potential for future applications.

Micro/nanomotors (MNMs) have attracted extensive attention because of their wide potential applications in diverse areas.[1–9] Due to the good catalytic activity in hydrogen peroxide (H_2O_2) decomposition, precious rare metal platinum (Pt) has always been the most widely used catalytic material to construct MNMs in different geometrical shapes, such as micro/nano-tubular engines,[10–12] Janus particles,[13,14] and bi-segment nanorods.[15] However, the scarcity, high cost and deactivation of Pt limit its further application. Hence, researchers are searching for new catalysts and propelling mechanisms for MNMs.[16] For examples, based on hydrogen bubbles generated by reactive metals with water and acids for propulsion, reactive MNMs have been generated but they exhibit very short lifetimes and the harsh reaction conditions limit their use in real applications.[17] Enzyme-based MNMs were also developed *via* a new propulsion strategy, because of the good catalytic performance over a wide range of biocatalytic reactions under mild environmental conditions.[18] Nevertheless, the enzyme based MNMs also suffer from quick deactivation in various media and harsh environments. The sophisticated synthetic procedures and low power output also hinder their future use.

MnO_2-based MNMs were developed to be an alternative to Pt, due to their low-cost, good propulsion, and robust nature.[16,19] Their polycrystallinity and various synthesis and modification methods provide good opportunities for researchers to design MnO_2 catalyzed MNMs.[20] By geometry design and crystallinity tuning, some MnO_2-based MNMs have been developed and tested.[21] Although fruitful achievements have been made, the performance of MnO_2 based MNMs still cannot compete with the Pt-based MNMs due to inferior catalytic performance.[22]

Herein we introduce a new catalyst for catalytic MNMs by modifying MnO_2 with mixed valence iron oxide (denoted as FeO_x–MnO_2) *via* cathodic electrochemical co-deposition. We fabricated graphene/FeO_x–MnO_2 bilayer tubular and rod-shaped micromotors, and evaluated their mobility performance. It is astounding to find that the newly designed micromotors move much faster than any reported MNMs at a low peroxide fuel concentration below 1% H_2O_2. What is more, these MnO_2 based MNMs exceed the fuel concentration range limit of the Pt-based MNMs by nearly an order of magnitude, reaching an extremely low value of 0.03% H_2O_2 with an acceptable speed of 89 ± 59 μm s^{-1}. Due to the easiness of fabrication, high catalytic performance, low cost, ecofriendly and biocompatible properties of the newly developed FeO_x–MnO_2 catalyst, we anticipate that a range of new MNMs based on this groundbreaking new strategy could be developed, and navigated at the very favorably low content of fuels to address diverse issues not limiting to the biomedical and environmental areas.

Scheme S1 (see ESI†) illustrates the fabrication process of the graphene/FeO_x–MnO_2 micromotors. These bilayer micromotors were constructed *via* a two-step electrochemical deposition process. Firstly, an outer layer of electrochemically reduced graphene oxide (erGO) was formed by deposition of graphene oxide into the pores of the membrane using a cyclic voltammetry

[a] *Department of Chemical Engineering, Curtin University, GPO Box U1987, Perth, Western Australia, 6845, Australia. E-mail: shaobin.wang@curtin.edu.au*
[b] *Key Lab of Advance Materials Technology of Educational Department Liaoning Province, Shenyang University, Shenyang, 110044, China*
[c] *School of Engineering, Edith Cowan University, 270 Joondalup Drive, Joondalup, Western Australia, 6027, Australia. E-mail: h.sun@ecu.edu.au*

† Electronic supplementary information (ESI) available: Experimental section, additional figures, tables and videos. See DOI: 10.1039/c8cc01548a

(CV) method.[23] Secondly, an inner layer of the FeO_x–MnO_2 catalyst was produced *via* cathodic electrochemical co-deposition. The electrochemical reductions of MnO_4^- ions and Fe^{3+} ions occur simultaneously. The synthetic parameters can be tailored to obtain rod-shaped and tubular micromotors.

Fig. 1 indicates that erGO/FeO_x–MnO_2 micromotors in microtube and microrod are fabricated successfully. Compared with the smooth tubular microengines, the inner surface of the erGO/FeO_x–MnO_2 microengines exhibits a larger surface area of electrochemical active sites for improving the catalytic activity.[24] The co-deposition of iron oxide and MnO_2 generates a much thinner wall. As shown in Fig. 1A and B, the wall thickness of the tubular micromotors is far less than 1 μm, which demonstrates its good mechanical properties. Without good mechanical strength, these tiny micro structures are very easy to be torn apart or crushed into pieces. This implies that the doping of iron oxide improves the mechanical strength of the micromotors, allowing the formation of the thin wall structured tubular micromotors with good structural integrity. The uniform distribution of carbon, oxygen, manganese, and iron demonstrates that the inner layer of iron oxide doped MnO_2 was fabricated successfully with good coverage by the outer graphene layer.

As illustrated in Fig. 2, XPS survey further reveals the presence of carbon (C 1s peak), oxygen (O 1s peak), manganese (Mn 2p peaks) and iron (Fe 2p peaks). The results are in good agreement with the SEM and EDX results. The peaks of high-resolution C 1s (Fig. 2B) and O 1s spectra (Fig. S1, ESI†) correspond to the binding energy of various functional groups, such as C–/C–H/C═C, C–OH, C═O, and O–C═O, revealing the nature of the covalent bonds of oxygen and carbon atoms.[25]

The quantities of the various functional groups are summarized in Table S1 (ESI†). The ratio of sp^2 carbons is at 68.33%, which indicates the degree of oxidation of the outer layer of the micromotor. Due to a higher cathode current for the reduction of the iron oxide doped MnO_2 catalyst, the oxidation degree is much lower than our previously designed MnO_2 based micromotors, which means that more graphene carbon lattices are recovered by the cathode galvanostatic electroreduction.[26] The high-resolution Mn 2p XPS spectra reveal the oxidation state of Mn (Fig. 2C). The peaks observed at the binding energies of 642.49 and 653.93 eV were attributed to the Mn 2p with the spin–orbit splitting of 11.44 eV. The Mn $2p_{3/2}$ peak located at 642.49 eV indicates the main oxidation state of Mn^{4+}.[26] Fig. 2D shows the high-resolution XPS spectra of Fe 2p for the iron oxide doped MnO_2 micromotors. The peaks at binding energies of 710.9 and 724.2 eV correspond to Fe $2p_{3/2}$ and Fe $2p_{1/2}$, respectively.[27] It can be noted that the Fe atomic distribution is a mixture of Fe^{2+} (710.9 eV) and Fe^{3+} (713.9 eV) with 77.5% of the iron species as Fe^{2+}.[28] Due to the electrochemical reduction process, Fe^{2+} ions are generated, but no zero valence iron (the Fe^0 peak usually exists at around 707.1 eV) was generated. Instead, a small proportion of Fe^{3+} was also doped into the MnO_2 matrix, as shown by the peak around 713.9 eV. Hence, the inner layer catalyst can be denoted as mixed valence iron doped MnO_2.

As demonstrated in Fig. 3A, the speed of all the micromotors exhibits an increasing tendency over the entire H_2O_2 fuel range with 1% sodium dodecyl sulfate (SDS) as a surfactant. The tubular micromotors demonstrate exceptionally high performance at extremely low peroxide levels. The speed of the erGO/FeO_x–MnO_2 tubular micromotors is 4 times faster than that of the erGO/Pt micromotors (187 ± 80 *vs.* 37 ± 10 μm s^{-1}) in 0.1% H_2O_2, which is the minimal fuel requirement for the best reported Pt catalyzed micromotors.[23] What's more, the erGO/FeO_x–MnO_2 micromotors can easily utilize the even lower fuel concentration of 0.03% H_2O_2 with a speed of 89 ± 59 μm s^{-1}, which is more than two-fold the speed of the erGO/Pt micromotors at a much higher fuel concentration of 0.1% H_2O_2.

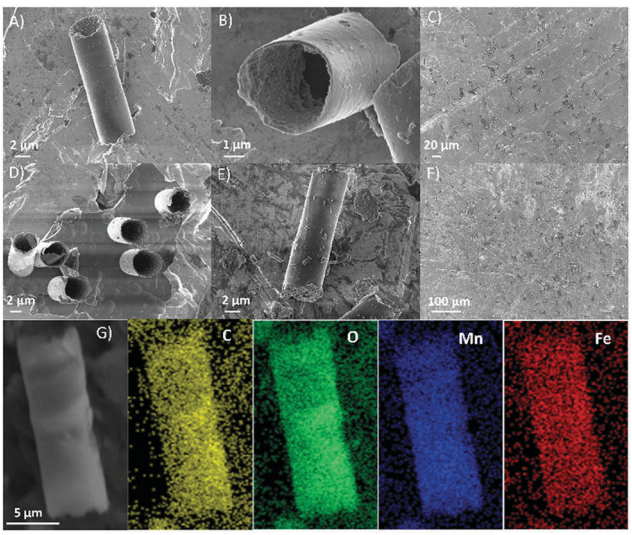

Fig. 1 Scanning electron microscopy (SEM) and energy dispersive X-ray (EDX) mapping analysis of the erGO/FeO_x–MnO_2 micromotors: (A) a lying microtube, (B) an upright microtube, (C) a number of microtubes, (D) an array of microtubes, (E) a lying microrod, (F) a number of microrods, and (G) EDX mapping analysis of a microtube.

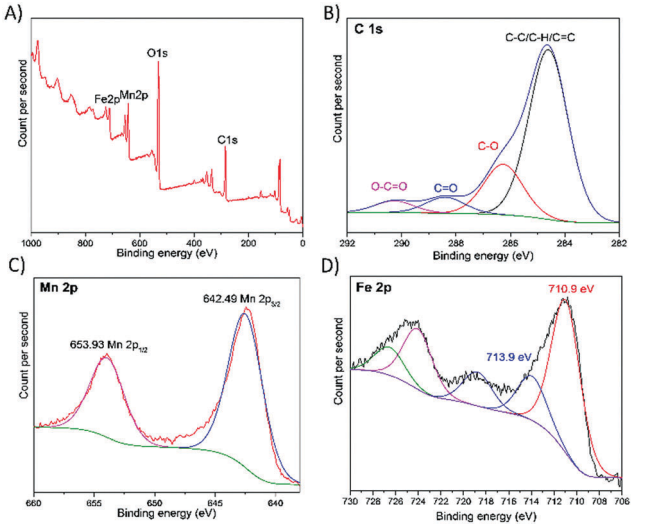

Fig. 2 XPS survey of the erGO/FeO_x–MnO_2 micromotors. (A) A wide scan showing Mn 2p, O 1s, C 1s and Fe 2p peaks. (B) High-resolution C 1s XPS spectra displaying various functional groups identified on the surface. (C) High-resolution Mn 2p XPS spectra. (D) High-resolution Fe 2p XPS spectra.

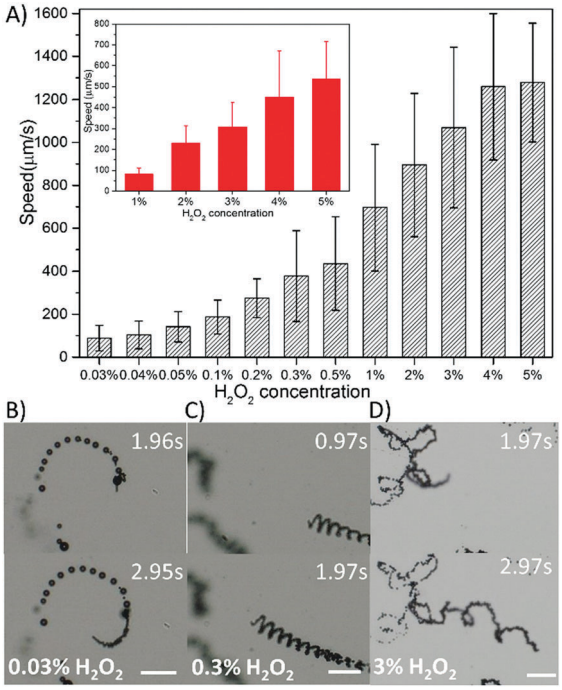

Fig. 3 Speed profile of erGO/FeO_x–MnO_2 micromotors in 1% SDS (n = 50). Average speed of tubular micromotors (inset: rod-shape micromotor) (A); time lapse images of tubular micromotors in 0.03% (B), 0.3% (C), and 3% (D) H_2O_2 extracted from the ESI,† Videos S1–S3. (Scale bars: 100 μm.)

Moreover, the minimal fuel content is two orders of magnitude lower than the 3% value of the graphene/MnO_2 micromotors.[26] At a slightly higher fuel concentration of 3%, the erGO/FeO_x–MnO_2 micromotors can easily exceed 1 mm s^{-1}, which is also remarkably high compared with polymeric/Pt micromotors, PANI/Pt, PPy/Pt, and PEDOT/Pt, which cannot exceed 1 mm s^{-1} in 3% H_2O_2.[24] The erGO/FeO_x–MnO_2 micromotors also exceed the speed of all the Pt based rolled-up multi-layer tubular micromotors and Janus motors at a relatively higher fuel content.[10,29] As shown in Fig. 3B, the tubular micromotors show circular motion behaviors at 0.03% H_2O_2. Ultra fast helical and irregular motion behaviors were also observed (Fig. 3C and D). As far as we know, Pt based micromotors require at least 0.1% H_2O_2 for propulsion, and MnO_2 based micromotors demand an even higher fuel concentration, while we demonstrate here that the Pt-free mixed valence iron oxide doped MnO_2 catalyzed micromotors could extend the fuel concentration to a very low threshold value of 0.03% with an acceptable velocity. The ground-breaking new catalyst along with the simple and low-cost fabrication method provides a new strategy to fabricate MNMs and will greatly boost motion in the tiny world.

As the surfactant is indispensable for the motion of bubble propelled tubular MNMs, the effect of the surfactant on the motion of FeO_x–MnO_2 micromotors could provide an insight for us to manipulate the motion behaviors.[30,31] Hence we investigated the mobility of the micromotors in 1%, 0.5%, and 0.05% H_2O_2 with different SDS concentrations, as shown in Fig. 4A–C, respectively.

At an extremely low content of the surfactant, the micromotors could not move, while at a very high content of the surfactant,

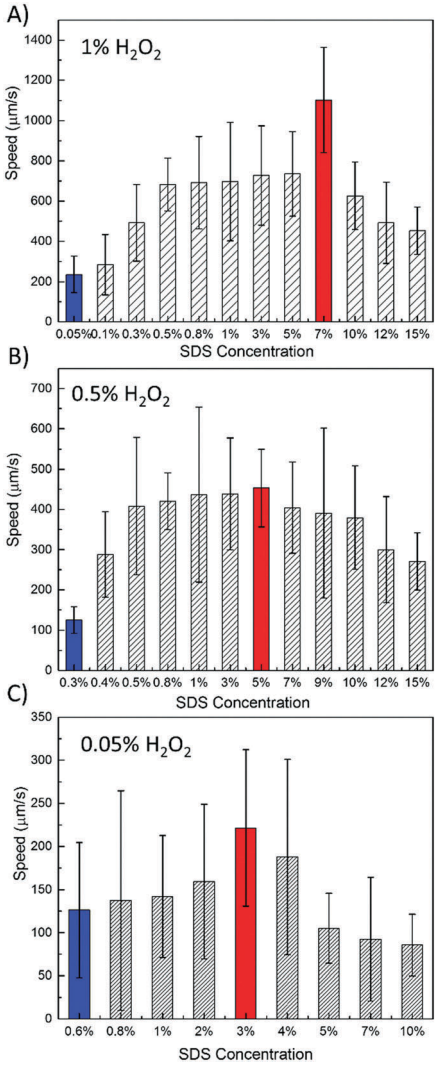

Fig. 4 Dependence of average speed of erGO/FeO_x–MnO_2 micromotors with varying SDS contents in 1% H_2O_2 (A), 0.5% H_2O_2 (B), and 0.05% H_2O_2 (C) (n = 50).

the high viscosity of the fluid would have an adverse effect on the motion to decrease the speed of micromotors. Hence, the minimal and optimal SDS surfactant contents for the micromotors at certain H_2O_2 fuel contents are important. As shown in Fig. 4, the blue bar corresponds to the minimal SDS concentration, while the red bar corresponds to the optimal surfactant content. It is interesting to note that as the fuel concentration drops from 1% to 0.05%, the minimal SDS concentration increases from 0.05% at 1% H_2O_2 to 0.3% at 0.5% H_2O_2 and finally reaches 0.6% at 0.05% H_2O_2. Meanwhile, the optimal SDS concentrations are 7%, 5%, and 3%, respectively. Under the optimized conditions, the speed of the erGO/FeO_x–MnO_2 tubular micromotors are 1102 ± 262 μm s^{-1}, 453 ± 97 μm s^{-1}, and 222 ± 91 μm s^{-1} in 1%, 0.5%, and 0.05% H_2O_2, respectively. The higher performance is usually obtained at moderate surfactant concentrations. This phenomenon can be used in sensing, detection, and motion based analysis. To the best of our knowledge, the unveiled high speed mobility properties at this low

content of fuels far exceed other reported MNMs under the same fuel conditions (Table S2, ESI†). As the toxicity of high concentration of H_2O_2 fuels is the major obstacle for biomedical applications, the iron modified manganese oxide MNMs will show a good prospect in biomedical and environmental applications due to the lower toxicity of the MNMs. The new types of MNMs provide a route to minimize the use of toxic fuel and surfactants and thus pave the way for biomedical applications, such as drug delivery. This new strategy could also minimize the environmental impact as lower contents of fuel and surfactants are needed for efficient motion.

For such fascinating mobility performance of this new-type of microengine, several effects take place. First and most importantly, the mixed valence iron doped MnO_2 catalyst exhibits a much high catalytic activity for H_2O_2 decomposition to produce oxygen, which gives faster generation and ejection of microbubbles. The rough inner catalytic layer also contributes to the improved catalytic performance. Secondly, the improved mechanical strength of the FeO_x–MnO_2 catalyst allows for the formation of a thin-walled tubular structure, thus significantly reducing the weight of the micromotors. Thirdly, the big difference in density between the iron oxide modified MnO_2 (usually the density is ≈ 5 g cm^{-3}) and Pt (the density is ≈ 20 g cm^{-3}) makes MnO_2 based MNMs much lighter than Pt-based tubular microengines. Fourthly, the ultra-thin wall of the graphene/FeO_x–MnO_2 tubular microengines would facilitate the fluid flow in the microtubes and minimize the effect of fluid resistance. Therefore, the structure design of the thin wall and the improved catalytic performance of the tubular microengines resulted in the exceptional high mobility at extremely low peroxide levels.

In conclusion, we demonstrate the first example of tubular microengines that propel efficiently by the thrust of oxygen bubbles in an extremely low H_2O_2 level (0.03%), which is nearly an order of magnitude lower than the previously reported values at above 0.2%. At below 1% of H_2O_2 fuel, the graphene/FeO_x–MnO_2 micromotors can move at far higher speeds than any reported MNMs. Such high-performance, low-cost micromotors could greatly expand the research and applications of micro/nano-scale motion tools and devices, and could thus lead to new biomedical and environmental applications for drug delivery or biological entity manipulation and environmental cleaning. In addition, the doping fabrication strategy provides a new approach for the designing of new types of MNMs.

The authors acknowledge the facilities and the scientific and technical assistance of the Australian Microscopy & Microanalysis Research Facility at the Centre for Microscopy, Characterization & Analysis, the University of Western Australia, a facility funded by the University, State and Commonwealth Government. The authors acknowledge the use of equipment, scientific and technical assistance of the WA X-ray Surface Analysis Facility, funded by the Australian Research Council LIFE Grant LE120100026.

Conflicts of interest

There are no conflicts to declare.

References

1 Y. F. Tu, F. Peng and D. A. Wilson, *Adv. Mater.*, 2017, **29**, 1701970.
2 F. Peng, Y. Tu and D. A. Wilson, *Chem. Soc. Rev.*, 2017, **46**, 5289–5310.
3 K. K. Dey and A. Sen, *J. Am. Chem. Soc.*, 2017, **139**, 7666–7676.
4 J. X. Li, I. Rozen and J. Wang, *ACS Nano*, 2016, **10**, 5619–5634.
5 H. Wang and M. Pumera, *Chem. Rev.*, 2015, **115**, 8704–8735.
6 S. Sanchez, L. Soler and J. Katuri, *Angew. Chem., Int. Ed.*, 2015, **54**, 1414–1444.
7 W. Duan, W. Wang, S. Das, V. Yadav, T. E. Mallouk and A. Sen, *Annu. Rev. Anal. Chem.*, 2015, **8**, 311–333.
8 M. Guix, C. C. Mayorga-Martinez and A. Merkoci, *Chem. Rev.*, 2014, **114**, 6285–6322.
9 W. Gao and J. Wang, *ACS Nano*, 2014, **8**, 3170–3180.
10 K. Yao, M. Manjare, C. A. Barrett, B. Yang, T. T. Salguero and Y. Zhao, *J. Phys. Chem. Lett.*, 2012, **3**, 2204–2208.
11 W. Gao, S. Sattayasamitsathit, J. Orozco and J. Wang, *J. Am. Chem. Soc.*, 2011, **133**, 11862–11864.
12 S. Sanchez, A. N. Ananth, V. M. Fomin, M. Viehrig and O. G. Schmidt, *J. Am. Chem. Soc.*, 2011, **133**, 14860–14863.
13 J. Orozco, L. A. Mercante, R. Pol and A. Merkoci, *J. Mater. Chem. A*, 2016, **4**, 3371–3378.
14 X. Ma, K. Hahn and S. Sanchez, *J. Am. Chem. Soc.*, 2015, **137**, 4976–4979.
15 U. K. Demirok, R. Laocharoensuk, K. M. Manesh and J. Wang, *Angew. Chem., Int. Ed.*, 2008, **47**, 9349–9351.
16 H. Wang, G. J. Zhao and M. Pumera, *J. Am. Chem. Soc.*, 2014, **136**, 2719–2722.
17 J. Li, V. V. Singh, S. Sattayasamitsathit, J. Orozco, K. Kaufmann, R. Dong, W. Gao, B. Jurado-Sanchez, Y. Fedorak and J. Wang, *ACS Nano*, 2014, **8**, 11118–11125.
18 X. Ma, A. C. Hortelao, A. Miguel-Lopez and S. Sanchez, *J. Am. Chem. Soc.*, 2016, **138**, 13782–13785.
19 M. Safdar, O. M. Wani and J. Janis, *ACS Appl. Mater. Interfaces*, 2015, **7**, 25580–25585.
20 O. M. Wani, M. Safdar, N. Kinnunen and J. Janis, *Chem. – Eur. J.*, 2016, **22**, 1244–1247.
21 M. Safdar, T. D. Minh, N. Kinnunen and J. Janis, *ACS Appl. Mater. Interfaces*, 2016, **8**, 32624–32629.
22 X. He, Y. K. Bahk and J. Wang, *Chemosphere*, 2017, **184**, 601–608.
23 A. Martin, B. Jurado-Sanchez, A. Escarpa and J. Wang, *Small*, 2015, **11**, 3568–3574.
24 W. Gao, S. Sattayasamitsathit, A. Uygun, A. Pei, A. Ponedal and J. Wang, *Nanoscale*, 2012, **4**, 2447–2453.
25 D. Vilela, J. Parmar, Y. Zeng, Y. Zhao and S. Sanchez, *Nano Lett.*, 2016, **16**, 2860–2866.
26 H. Ye, H. Q. Sun and S. B. Wang, *Chem. Eng. J.*, 2017, **324**, 251–258.
27 J. Parmar, D. Vilela, E. Pellicer, D. Esqué-de los Ojos, J. Sort and S. Sánchez, *Adv. Funct. Mater.*, 2016, **26**, 4152–4161.
28 Z. Jia, X. G. Duan, P. Qin, W. C. Zhang, W. M. Wang, C. Yang, H. Q. Sun, S. B. Wang and L. C. Zhang, *Adv. Funct. Mater.*, 2017, **27**, 1702258.
29 X. Ma, J. Katuri, Y. Zeng, Y. Zhao and S. Sanchez, *Small*, 2015, **11**, 5023–5027.
30 J. Simmchen, V. Magdanz, S. Sanchez, S. Chokmaviroj, D. Ruiz-Molina, A. Baeza and O. G. Schmidt, *RSC Adv.*, 2014, **4**, 20334–20340.
31 H. Wang, G. J. Zhao and M. Pumera, *J. Phys. Chem. C*, 2014, **118**, 5268–5274.

